Taylor Couette Instability in Disk Suspensions: Experimental Observation and Theory

J. J. J. Gillissen[1], N. Cagney[2,3], T. Lacassagne[3],
A. Papadopoulou[3], S. Balabani[3] and H. J. Wilson[1]

[1] *Department of Mathematics, University College London, Gower Street, London WC1E 6BT, United Kingdom*

[2] *School of Engineering and Materials Science, Queen Mary University of London, United Kingdom*

[3] *Department of Mechanical Engineering, University College London, United Kingdom*[*]

(Dated: March 30, 2020)

Abstract

Using the well-known hydrodynamic theory for dilute suspensions of spheroids, we have previously predicted the destabilisation of Taylor Couette flow, due to anisotropic viscous stresses induced by suspended disk-shaped particles [1]. Here we provide experimental evidence for the destabilisation mechanism using suspensions of mica flakes. As a function of the mica concentration, there is good qualitative agreement between the experiment and the theory in the concentration dependence of the critical speed for instability onset and of the axial wavelength of the corresponding Taylor vortices. Quantitative differences are attributed to hydrodynamic interactions between the disks, which we account for in the theory in an ad-hoc fashion using rotary diffusion.

[*] jurriaangillissen@gmail.com

I. INTRODUCTION

Taylor Couette flow (TCF) is the flow in the gap between two counter rotating cylinders. When the outer cylinder is held fixed, and the rotation speed of the inner cylinder exceeds a threshold value, the circular Taylor Couette base flow destabilises, which is accompanied by the emergence of so-called Taylor vortices [2]. For Newtonian fluids, the onset of instability corresponds to the Taylor number:

$$\mathrm{Ta} = \frac{\rho\Omega\sqrt{\Delta R^3 R_1}}{\eta_s}, \tag{1}$$

exceeding a critical value Ta_c that depends on the cylinder radius ratio R_1/R_2. Here η_s is the fluid viscosity, Ω is the angular velocity of the inner cylinder, $\Delta R = R_2 - R_1$ is the gap width between the cylinders, and R_1 and R_2 are the radii of the inner and of the outer cylinder, respectively.

In non-Newtonian fluids the behaviour is different, and two types of non-Newtonian TCF instabilities have been observed. The first type is driven by centrifugal forces, similar to the Newtonian instability, described above. In this case the non-Newtonian rheology only alters the details of the instability, i.e. the onset speed, the shape and the dynamics of the Taylor vortices, while the driving force remains the same. Examples of this type of instability include fluids with a shear thinning rheology [3–5] or suspensions of rod-like polymers, e.g. polyacrylic acid, xanthan and carboxymethyl cellulose [1, 6–8]. Other examples include dense suspensions of spheres [9–11], where non-Newtonian effects may arise from an anisotropic microstructure [12–15] as well as from a heterogeneous solid concentration [9, 16].

The second type of non-Newtonian TCF instability is driven by viscoelastic stresses and persists even in the absence of centrifugal forces. This so-called "elastic instability" has been observed in polymer solutions: [17–19] and in micelle solutions [20] where in the later case, the instability is also affected by shear banding, i.e. by a non-monotonic relationship between the stress and the strain rate. The elastic instability is well understood and reproduced by numerical simulation using constitutive equations of viscoelastic fluids [18, 21].

In this work we report on the modification of the centrifugal TCF instability, due to anisotropic viscous stresses generated by suspended disk-shaped particles. It is noted that dilute suspensions of spherical particles (with volume fraction $c \lesssim 0.05$) behave as Newtonian fluids with an elevated viscosity. In this regard it is noted that for $c \lesssim 0.05$, spherical particles may induce a very small destabilising effect, which may be attributed to particle inertia [16].

In a previous work we theoretically studied the destabilising effect of anisotropic viscous stresses induced by disk-shaped particles [1]. In that work we predicted that for suspensions of perfectly aligned disks, i.e. disk with an infinite aspect ratio and zero rotary diffusivity D_r, the instability persists even when the centrifugal force becomes vanishingly small. Zero rotary diffusion corresponds to an infinite rotary Péclet number:

$$\mathrm{Pe} = \frac{\dot{\gamma}}{D_r}. \tag{2}$$

Here $\dot{\gamma}$ is the shear rate and $D_r \sim k_B T/(\eta_s l^3)$ where l is the major axis of the disks. It was indeed predicted that under these idealised conditions, the critical Taylor number [Eq. (1)], required for instability onset, was equal to zero. It was furthermore shown that, as $\mathrm{Ta} \to 0$, the instability growth rate λ decreases as $\lambda \sim \nu \Delta R^{-2} \mathrm{Ta}^2$ (Fig. 4b in Ref. [1]), i.e. a non-zero growth rate also requires a non-zero centrifugal force.

A related but not entirely similar destabilisation mechanism has been observed in suspensions of disk-shaped clay particles [22]. These clay suspensions however generate elastic stresses and are shear thinning due to rotary diffusion and electrostatic inter-particle forces [23]. These effects destabilise TCF even in the absence of anisotropic viscous stresses [3].

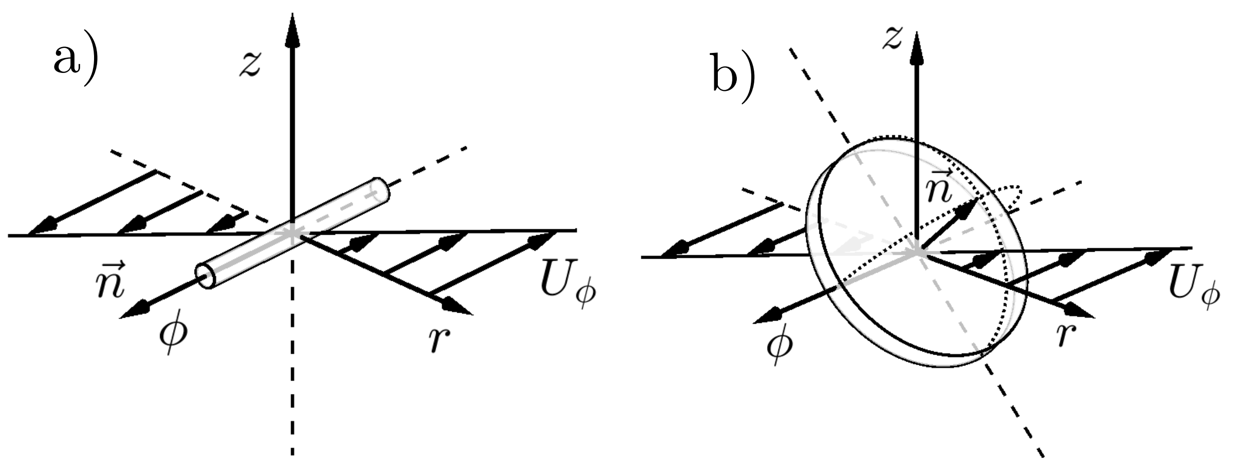

FIG. 1. (a) A rod with its major axis $\boldsymbol{n}$ in the azimuthal direction ϕ, does not rotate when subjected to an azimuthal vorticity perturbation. (b) A disk on the other hand tilts its normal $\boldsymbol{n}$ away from the radial direction r towards the axial direction z. The mean flow field $U_\phi(r)$ is drawn relative to the motion of the particles.

We explain the destabilising effect of suspended disks, by contrasting it to the negligible

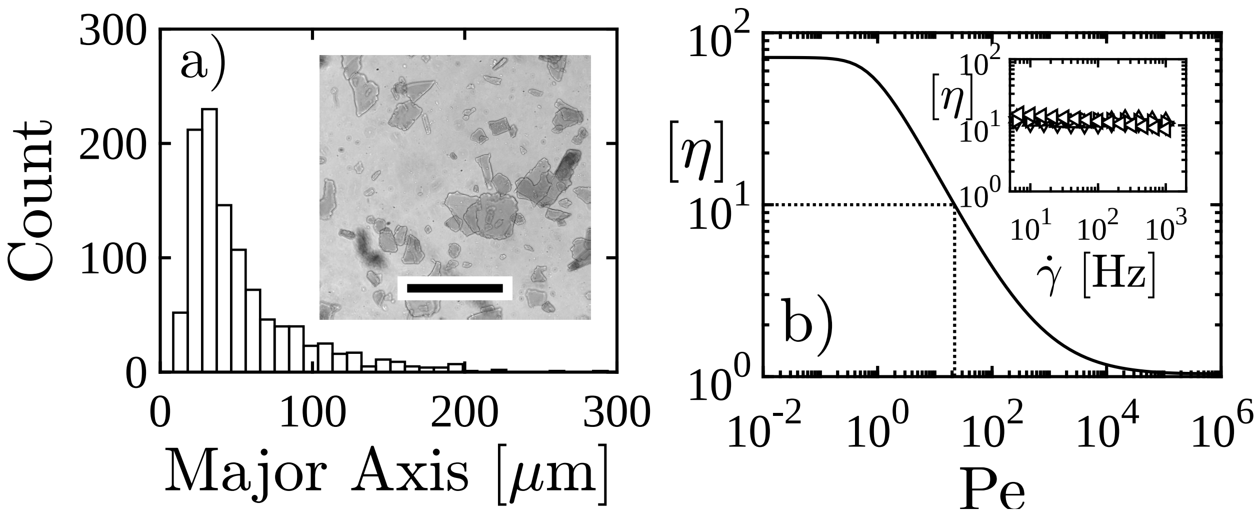

FIG. 2. (a) Mica size distribution, obtained from micrographs, as shown in the inset which has a 200 μm scale bar. (b) The theoretical, intrinsic viscosity $[\eta]$ as a function of the rotary Péclet number Pe in dilute suspensions of disks with an aspect ratio of $r_a^{-1} = 10^2$. The dotted lines indicate the rotary Péclet value $\mathrm{Pe} \approx 22$ that corresponds to the measured $[\eta] \approx 10$. The inset shows the experimentally measured intrinsic viscosity in mica suspensions as a function of the shear rate, for $c = 5 \times 10^{-3}$ (downward triangle), $c = 10^{-2}$ (upward triangle), $c = 2 \times 10^{-2}$ (rightward triangle) and $c = 5 \times 10^{-2}$ (leftward triangle).

effect of suspended rods. Fig. 1a illustrates a rod in the Taylor Couette base flow which has a strain rate $s_{\phi r}$. The flow, gradient and vorticity directions are ϕ, r and z, respectively. In the limit of an infinite aspect ratio and an infinite Péclet number [Eq. (2)], the rod major axis $\boldsymbol{n}$ points in the ϕ-direction and generates no additional stress. A Taylor vortex perturbation corresponds to azimuthal fluid vorticity ω'_ϕ, i.e. to fluid rotation around $\boldsymbol{n}$. Consequently $\boldsymbol{n}$ remains fixed and the rod generates no hydrodynamic stress.

For a disk, the situation is sketched in Fig. 1b. In the base flow, the disk normal $\boldsymbol{n}$ points in the r-direction. A Taylor vortex perturbation ω'_ϕ rotates $\boldsymbol{n}$ away from the r-axis and towards the z-axis. The perturbation of the disk normal in the z-direction n'_z generates a stress perturbation $\sigma'_{\phi z} \sim s_{\phi r} n_r n'_z$ [Eq. (9) below]. This stress perturbation has an amplifying feedback on the Taylor vortex perturbation ω'_ϕ via $\partial_t u'_\phi \sim \partial_z \sigma'_{\phi z}$ and $\partial_t u'_r \sim (U/R) u'_\phi$ [Eq. (8) below] and $\omega'_\phi \sim \partial_z u'_r$.

II. EXPERIMENTS

In this work we provide experimental evidence for the destabilising effect of TCF due to suspended, non-Brownian and (nearly) non-adhesive disks. To this end we use suspensions of mica flakes (Cornellius Ltd.) with a thickness of $d \approx 1$ μm and a mass density of 2.93 g cm^{-3}. Fig. 2a shows the distribution of the major particle axis l which is obtained from 20 micrographs, as shown in the inset of Fig. 2a. In addition to inducing hydrodynamic instability, the mica flakes also serve to visualise the flow structures. The reflectivity of the suspension depends on the relative orientation of the incoming and the outgoing light w.r.t to the orientation of the flakes, which in turn is governed by the various components of the fluid velocity gradient tensor [see Eq. (10) below].

We examine one Newtonian fluid, i.e. with a very low flake concentration $c = 10^{-4}$, and five suspensions with flake volume fractions ranging between $c = 10^{-3}$ and $c = 5 \times 10^{-2}$. The suspending medium is a mixture of glycerol (volume fraction G), distilled water (volume fraction W) and aqueous food dye to aid flow visualisation (volume fraction 0.02). For $c \leq 10^{-2}$ and $c \geq 2 \times 10^{-2}$ we used (G,W) = (0.71, 0.27) and (0.9, 0.08) respectively, which correspond to a density and a viscosity of (ρ [g cm^{-3}], η_s [Pa s]) of (1.18, 0.036) and (1.24, 0.3), respectively. Here the more viscous liquid was used to suppress sedimentation effects at the higher mica concentrations.

The steady shear viscosity η_{eff} of the suspensions is measured using a rotational rheometer (TA Instruments) equipped with a cone-and-plate geometry. The inset of Fig. 2b shows the measured intrinsic viscosity:

$$[\eta] = \frac{\eta_{\text{eff}} - \eta_s}{c\eta_s}, \tag{3}$$

as a function of the shear rate $\dot{\gamma}$ for the various suspensions. The shear rate range $5 \leq \dot{\gamma} \leq 10^3$ s^{-1} would correspond to a Taylor number [Eq. (1)] range in the TCF setup of approximately $3 \leq \text{Ta} \leq 6 \times 10^2$. The measured $[\eta]$ collapse for the various c, i.e. $[\eta]$ is independent of c, causing overlapping (and therefore invisible) markers in the inset of Fig. 2b. Moreover, for $c \leq 2 \times 10^{-2}$ we see that $[\eta]$ is independent of $\dot{\gamma}$, and for $c = 5 \times 10^{-2}$ there is slight shear thinning $[\eta] \sim \dot{\gamma}^{-0.02}$. The suspensions are therefore (nearly) rate independent, which confirms absence of adhesion forces and the corresponding elastic behaviour.

The cylinders in the TCF setup have length $L = 155$ mm and radii $R_1 = 21.66$ mm and $R_2 = 27.92$ mm which correspond to a radius ratio of $R_1/R_2 = 0.77$ and an aspect ratio of $L/\Delta R = 21.56$. The flow cell is enclosed within a rectangular chamber in which water is recirculated, to keep the fluid temperature in the flow cell at 20 ± 0.1°C [5]. The inner cylinder is accelerated from rest with a constant $\mathrm{d}\Omega/\mathrm{d}t$. The flow cell is illuminated using a white light-emitting diode (SugarCUBE, Edmund Optics). We image a strip of the flow cell with a CMOS camera (Phantom Miro 340) at a frame rate of 60 s^{-1} and a resolution of 2224×16 pixels in the z and ϕ directions. Each image is averaged over the 16 pixels in the lateral (ϕ) direction, into an axial profile with 2224 pixels. The resulting profiles are combined into a matrix which is referred to as the light intensity map $I(z, \mathrm{Ta})$. This map is a function of the height z and of the effective Taylor number Ta:

$$\mathrm{Ta} = \frac{\rho\Omega\sqrt{\Delta R^3 R_1}}{\eta_{\mathrm{eff}}}. \tag{4}$$

Here η_{eff} is the measured, effective viscosity; see inset of Fig. 2b.

In Fig. 3 we show $I(z, \mathrm{Ta})$ for mica concentrations ranging from $c = 10^{-4}$ to $c = 5 \times 10^{-2}$. The figure shows that, above a critical Taylor number Ta_c, the circular base flow transitions into a vortical flow, indicated by the appearance of bright and dark bands in $I(z, \mathrm{Ta})$. These bands are (nearly) horizontal which shows that the vortices are axisymmetric and non-oscillatory.

For the Newtonian suspension, with negligible mica concentration $c = 10^{-4}$ (Fig. 3a), the instability starts at both ends in the form of Ekman vortices. Since these end effects are not associated with the Taylor vortices, we disregard the end regions in the subsequent analysis. For $c = 5 \times 10^{-2}$ (Fig. 3d) sedimentation effects are manifested by the dark region in the lower half. These regions are also disregarded from the subsequent analysis.

In the more concentrated suspensions (Figs. 3b-d) faint ridges appear for $\mathrm{Ta} > \mathrm{Ta}_c$ which gradually become more distinct as Ta is increased further. This indicates that at $\mathrm{Ta} = \mathrm{Ta}_c$ the Taylor vortex strength is relatively weak and it grows for $\mathrm{Ta} > \mathrm{Ta}_c$. This gradual development of the Taylor vortex strength is not observed in the Newtonian system (Fig. 3a) nor in similar measurements of solutions of flexible or rod-like polymers; see e.g. Ref. [5].

The light intensity map for $c = 10^{-2}$ in Fig. 3b shows another interesting feature; as Ta is increased, the number of vortices (indicated by the number of bright and dark bands) abruptly decreases at several points. These events correspond to the merger of two adjacent vortices. A close-up of such a vortex merger event is provided in the inset of Fig. 3b. This

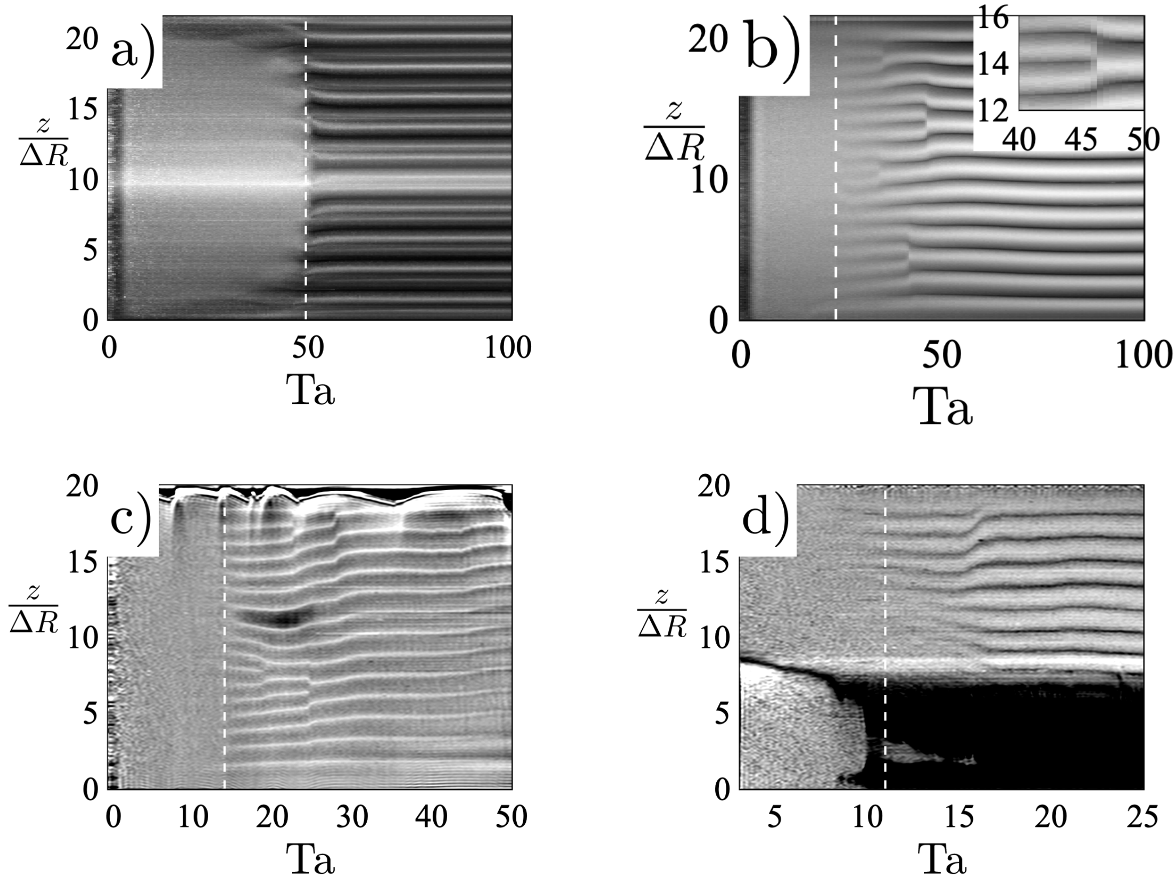

FIG. 3. Light intensity maps $I(z, \mathrm{Ta})$ using $\mathrm{d}\Omega^*/\mathrm{d}t^* \approx 0.7$ [Eq. (6)] for mica suspensions with concentrations of $c = 10^{-4}$ (a), $c = 10^{-2}$ (b), $c = 2 \times 10^{-2}$ (c) and $c = 5 \times 10^{-2}$ (d). The light intensity maps show the onset of instability as the appearance of the banded structures above a critical speed, indicated by the dashed white lines. The inset of (b) shows a close-up of a vortex merger event.

phenomenon has also been observed in solutions of polymers [5, 25]. It is noted that these sudden jumps are likely due to the finite $L/\Delta R$ of the TCF setup, while for $L/\Delta R \to \infty$ these changes are expected to be continuous.

The onset of instability corresponds to critical values, k_c and Ta_c, of the axial vortical wavenumber k and of the effective Taylor number [Eq. (4)]. To determine k_c and Ta_c. the $I(z, \mathrm{Ta})$ (Fig. 3) are first filtered over Ta with a filter-width of $\Delta\mathrm{Ta} \approx 1$. This is to improve the statistical significance of the variations of $I(z, \mathrm{Ta})$ with Ta. Then for each value of Ta,

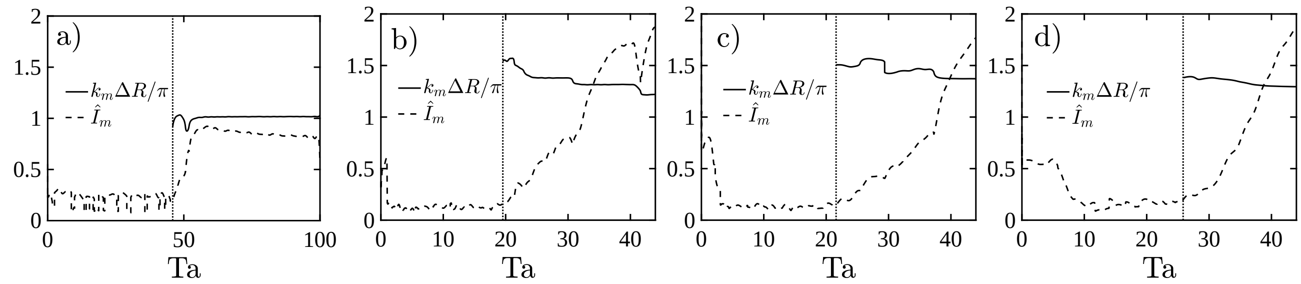

FIG. 4. The maximum $\hat{I}_m$ (arbitrary units) of the Fourier transformed light intensity map [Eq. (5)] and the corresponding wavenumber k_m as functions of Ta for $c = 10^{-4}$ and $\mathrm{d}\Omega^*/\mathrm{d}t^* \approx 0.7$ (a), and for $c = 10^{-2}$ and $\mathrm{d}\Omega^*/\mathrm{d}t^* \approx 0.1$ (b), $\mathrm{d}\Omega^*/\mathrm{d}t^* \approx 0.7$ (c) and $\mathrm{d}\Omega^*/\mathrm{d}t^* \approx 7$ (d). The critical Taylor number Ta_c is indicated with the vertical dotted lines, which correspond to the growth onset of $\hat{I}_m$.

we compute the Fourier transform:

$$\hat{I}(k, \mathrm{Ta}) = \int \exp(izk) I(z, \mathrm{Ta}) dz. \tag{5}$$

For each Ta we determine the maximum $\hat{I}_m$ of $\hat{I}(k, \mathrm{Ta})$ as a function of k, excluding the $k = 0$ mode. The maximum $\hat{I}_m$ occurs at wavenumber k_m.

Fig. 4a shows $\hat{I}_m$ and k_m as functions of Ta for the Newtonian system (Fig. 3a) using $c = 10^{-4}$ and a non-dimensional ramp-up speed of $\mathrm{d}\Omega^*/\mathrm{d}t^* \approx 0.7$ [26]:

$$\frac{\mathrm{d}\Omega^*}{\mathrm{d}t^*} = \frac{\rho^2 R_1 \Delta R^3}{\eta_{\mathrm{eff}}^2} \frac{\mathrm{d}\Omega}{\mathrm{d}t}. \tag{6}$$

As Ta passes the critical value Ta_c, indicated by the vertical dotted line, $\hat{I}_m$ starts growing which corresponds to the onset of Taylor vortices. We find a critical Taylor number of $\mathrm{Ta}_c \approx 46$ which is very close to the theoretical value of $\mathrm{Ta}_c \approx 48$ [24]. The critical wavenumber k_c is determined as k_m at $\mathrm{Ta} = \mathrm{Ta}_c$, which gives $k_c \Delta R/\pi \approx 0.92$, which is close to the theoretical value of $k_c \Delta R/\pi \approx 1.0$. The agreement between experimental results and literature values confirms that the non-dimensional ramp-up speed of $\mathrm{d}\Omega^*/\mathrm{d}t^* \approx 0.7$ is sufficiently slow to ensure quasi steady conditions, i.e. the results are not affected by the finite acceleration rate.

Figs. 4b-d show $\hat{I}_m$ and k_m as functions of Ta for $c = 10^{-2}$ (Fig. 3b) and for three values for $\mathrm{d}\Omega^*/\mathrm{d}t^*$. It can be seen that for $\mathrm{d}\Omega^*/\mathrm{d}t^* \approx 0.1$ and 0.7 the critical values Ta_c and k_c are close to one another, i.e. $\mathrm{Ta}_c \approx 19.7$ and 21.6 and $k_c \approx 1.55$ and 1.51, while for the larger

$\mathrm{d}\Omega^*/\mathrm{d}t^* \approx 7$, the critical values deviate somewhat, i.e. $\mathrm{Ta}_c \approx 26.0$ and $k_c \approx 1.38$. These results show that for $c = 10^{-2}$, $\mathrm{d}\Omega^*/\mathrm{d}t^* \approx 0.7$ is sufficiently slow to obtain critical values that are (nearly) independent of $\mathrm{d}\Omega^*/\mathrm{d}t^*$. It is finally noted that the vortical wavelength k_m in Figs. 4b-c show discontinuous jumps which are associated with the vortex merger events, as shown in Fig. 3b.

III. THEORY

We now compare the experimental results to the theoretical model of Ref. [1]. The model is based on the well-known constitutive equations for dilute suspensions of spheroids which are given by the continuity equation [27]:

$$\boldsymbol{\nabla} \cdot \boldsymbol{u} = 0, \tag{7}$$

and the momentum equation:

$$\rho \partial_t \boldsymbol{u} = \boldsymbol{\nabla} \cdot \left(-\rho \boldsymbol{u}\boldsymbol{u} - p\boldsymbol{\delta} + \eta_s \left(\boldsymbol{\nabla}\boldsymbol{u} + \boldsymbol{\nabla}\boldsymbol{u}^T \right) + \boldsymbol{\sigma} \right). \tag{8}$$

The spheroid stress $\boldsymbol{\sigma}$:

$$\frac{\boldsymbol{\sigma}}{\eta_s} = 2\alpha_1 \boldsymbol{s} + 2\alpha_2 \boldsymbol{s} : \boldsymbol{a}\boldsymbol{a} + \alpha_3 \left(\boldsymbol{s} \cdot \boldsymbol{a} + \boldsymbol{a} \cdot \boldsymbol{s} \right) + \alpha_4 D_r \left(\boldsymbol{a} - \tfrac{1}{3}\boldsymbol{\delta} \right), \tag{9}$$

depends on the microstructure $\boldsymbol{a} = \langle \boldsymbol{n}\boldsymbol{n} \rangle$. Here $\boldsymbol{n}$ is the unit vector along the spheroid polar axis and $\langle \cdots \rangle$ is the average that is weighted with the probability density function of $\boldsymbol{n}$. The microstructure tensor $\boldsymbol{a}$ evolves as:

$$\begin{aligned} \partial_t \boldsymbol{a} = -\boldsymbol{u} \cdot \boldsymbol{\nabla}\boldsymbol{a} + \boldsymbol{\nabla}\boldsymbol{u}^T \cdot \boldsymbol{a} + \boldsymbol{a} \cdot \boldsymbol{\nabla}\boldsymbol{u} \\ + (B-1)\left(\boldsymbol{s} \cdot \boldsymbol{a} + \boldsymbol{a} \cdot \boldsymbol{s} \right) - 2B\boldsymbol{s} : \boldsymbol{a}\boldsymbol{a} - D_r \left(\boldsymbol{a} - \tfrac{1}{3}\boldsymbol{\delta} \right). \end{aligned} \tag{10}$$

Here $\boldsymbol{u}$ is the velocity, ρ is the suspension mass density, p is the pressure, $\boldsymbol{s} = \frac{1}{2}\left(\boldsymbol{\nabla}\boldsymbol{u} + \boldsymbol{\nabla}\boldsymbol{u}^T \right)$ is the rate of strain tensor, D_r is the rotary diffusivity which is added to mimic the effects of hydrodynamic interactions between the non-Brownian disks, c is the spheroid volume fraction, $r_a = a/b$ is the aspect ratio, a is the polar radius b is the equatorial radius, α_i are material constants that depend on c and r_a and $B = (r_a^2 - 1)/(r_a^2 + 1)$. The cases: $r_a < 1$, $r_a = 1$ and $r_a > 1$ correspond to oblate spheroids (disks), spheres and prolate spheroids (rods), respectively.

In order to estimate the effective aspect ratio that corresponds to the size distribution in Fig. 2a, we use that the disk stress $\boldsymbol{\sigma}$ scales with the disk major axis cubed [27]. Therefore the relevant particle dimension is the cube root of the third moment of this distribution $l_{\text{eff}} = \langle l^3 \rangle^{1/3} \sim 10^2$ μm, giving an aspect ratio of $r_a^{-1} = l_{\text{eff}}/d \sim 10^2$.

In the dilute theory [Eqs. (7-10)] hydrodynamic interactions are not taken into account rigorously. The number of these interactions per particle is proportional to the volume fraction of the disk-circumscribing spheres $\sim cr_a^{-1}$. In the present work, we consider mica suspensions with concentrations up to $cr_a^{-1} \sim 5$, for which hydrodynamic interactions are expected to be important. We model these effects with the rotary diffusion terms (D_r terms) in Eqs. (9-10). Theoretical and experimental studies have shown that rotary diffusion is an adequate model for hydrodynamic interactions between rods [28–32]. For disks on the other hand there are no equivalent studies and at present it is not clear if interactions can adequately be modelled by rotary diffusion. Below, we shed some light on this issue by comparing the theoretical model [Eqs. (7-10)] to experimental data, for both steady shear flow and for the TCF instability.

First we show in Fig. 2b the theoretical [Eqs. (7-10)] intrinsic viscosity $[\eta]$ [Eq. (3)] in the steady shear flow of a suspension of oblate spheroids with an aspect ratio of $r_a^{-1} = 10^2$ as a function of the rotary Péclet number [Eq. (2)]. The theoretical viscosity in Fig. 2b decreases as a function of Pe. For Pe ≈ 22 the model matches the experimental data $[\eta] \approx 10$ (inset of Fig. 2b). We re-emphasise that the mica flakes are non-Brownian and that rotary diffusion is used as a model for the effects of hydrodynamic interactions between the disks. We further note that the (near) shear rate $\dot{\gamma}$ invariance of $[\eta]$ (inset in Fig. 2b) indicates a constant rotary Péclet number [Eq. (2)], i.e. $D_r \sim \dot{\gamma}$.

We now present linear stability analysis of the cylindrical coordinate version of Eqs. (7-10), with respect to axisymmetric perturbations $u'(r)\exp(\mathrm{i}kz)\exp(\lambda t)$ where k is the axial wavenumber and λ is the growth rate. The axisymmetry of the instability modes is experimentally observed in Figs. 3a-b. Details of the stability analysis are given in Ref. [1]. Briefly, we discretise Eqs. (7-10) using the Chebyshev collocation method on 30 collocation points. After computing the base state, we compute λ by numerically solving the corresponding generalised eigenvalue problem. All λ are found to be real-valued, i.e. non-oscillatory, in agreement with the experimental observations in Figs. 3a-b.

To match the experimental system, we use a radius ratio of $R_1/R_2 = 0.77$, a disk aspect

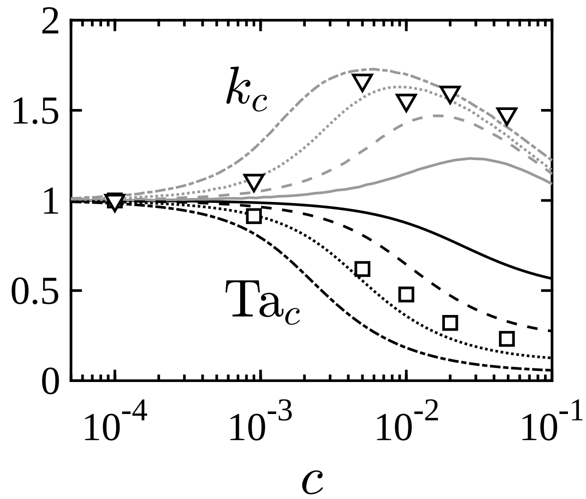

FIG. 5. The critical Taylor number Ta_c (black lines and squares) and the critical vortical wavenumber k_c (grey lines and triangles), normalised by their Newtonian values, plotted versus the disk concentration c. Comparison between experimental data (markers) using $\mathrm{d}\Omega^*/\mathrm{d}t^* \approx 0.7$ [Eq. (6)] and theory (lines) . The theory uses an aspect ratio of $r_a^{-1} = 10^2$ and a rotary Péclet number of $\mathrm{Pe} = 1 \times 10^2$ (solid lines), $\mathrm{Pe} = 1 \times 10^3$ (dashed lines), $\mathrm{Pe} = 1 \times 10^4$ (dotted lines) and $\mathrm{Pe} = 1 \times 10^5$ (dash-dotted lines).

ratio of $r_a^{-1} = 10^2$ and we vary the disk concentration between $c = 10^{-4}$ and $c = 10^{-1}$ and the rotary Péclet number between $\mathrm{Pe} = 10^2$ and $\mathrm{Pe} = 10^5$. For each c and Pe we vary the wavenumber k of the perturbation and for each k we vary the rotation speed Ω. We thereby find the critical wavenumber k_c and the critical Taylor number Ta_c that mark the transition between positive and negative λ, i.e. the onset of instability.

Fig. 5 shows good qualitative agreement between the computed and measured Ta_c and k_c as functions of c. The experimentally measured k_c show a slight discontinuity between $c = 10^{-2}$ and $c = 2 \times 10^{-2}$ which is likely due to the change in the suspending medium (see Sec. II) and the corresponding changes in sedimentation and inter-particle adhesion. These effects are considered weak, however, since the measured Ta_c (Fig. 5) does not show a discontinuity. The experimental data for Ta_c agree well with the numerical results for $10^3 \lesssim \mathrm{Pe} \lesssim 10^4$. This range is beyond the value of $\mathrm{Pe} \approx 22$, that was required to match the constitutive model to experiments for steady shear flow (Fig. 2b). This discrepancy highlights that rotary diffusion is not an accurate model for hydrodynamic interactions between disks. Indeed hydrodynamic interactions between disks are more complicated than a mere randomising effect. These interactions may also produce the opposite effect of suppressing rotation due to steric constraints [33]. Nevertheless there is good qualitative agreement between the theory and the experimental data, in both Ta_c and k_c as functions of c. This agreement supports our theoretical finding [1] that Taylor Couette flow can be destabilised by anisotropic viscous stresses due to suspended disks-shaped particles.

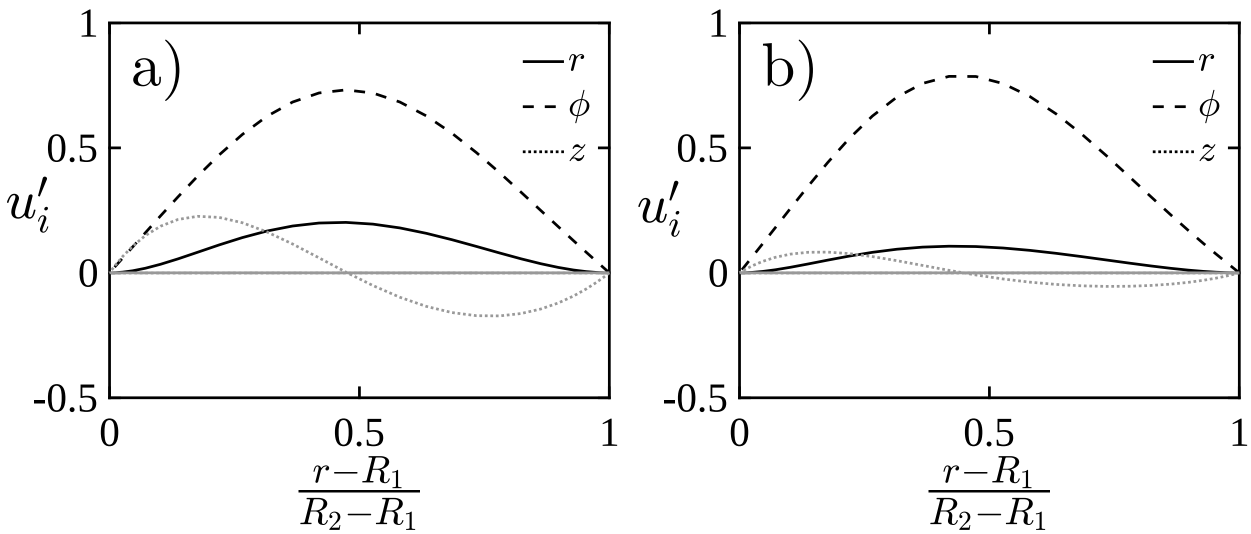

FIG. 6. Real part (black) and imaginary part (grey) of the theoretically computed Taylor vortex in a Newtonian system (a) and in a disk suspension (b), using an aspect ratio of $r_a^{-1} = 10^2$, a rotary Péclet number of $\mathrm{Pe} = 3 \times 10^3$ and a concentration of $c = 10^{-2}$.

Fig. 6 shows the theoretically computed velocity profiles of the Taylor vortices with $c = 0$ and $\mathrm{Ta} = \mathrm{Ta}_c \approx 48$ and with $c = 10^{-2}$ and $\mathrm{Ta} = \mathrm{Ta}_c \approx 24$. Compared to the Newtonian Taylor vortex (6a), the Taylor vortex in the disk suspension (6b) has a suppressed cross stream velocity. These results agree qualitatively with the light intensity maps in Fig. 3, showing that the Newtonian Taylor vortex has a relatively large intensity immediately at $\mathrm{Ta} = \mathrm{Ta}_c$ which stays roughly constant for $\mathrm{Ta} > \mathrm{Ta}_c$, whereas the non-Newtonian Taylor vortex, using $c = 10^{-2}$, has a relatively small intensity at $\mathrm{Ta} = \mathrm{Ta}_c$ which increases for $\mathrm{Ta} > \mathrm{Ta}_c$.

IV. CONCLUSIONS

We have previously theoretically predicted that Taylor Couette flow can be destabilised by anisotropic viscous stresses, induced by suspended disk-shaped particles [1]. These particles redirect the transfer of azimuthal momentum from the radial to the axial direction. The theory was based on the well-known constitutive equations of dilute, i.e. non-interacting, spheroid suspensions.

In this work we have provided experimental evidence for this destabilisation mechanism, using suspensions of mica flakes. In order to match the theory to the experimental data we have included a rotary diffusion term to the constitutive equations which models the hydrodynamic interactions between the disks. With this modification, there is good qualitative agreement between theory and experiment in the concentration dependence of the critical speed for instability onset and of the Taylor vortex size. Quantitative differences between the theory and the experiments reflect the imperfection of modelling hydrodynamic interactions using rotary diffusion.

This new destabilisation mechanism has a range of potential industrial applications, e.g. to enhance mixing in chemical reactors or to enhance heat transfer in drilling equipment.

---

[1] J. Gillissen and H. Wilson, Phys. Rev. Fluids **3**, 113903 (2018).

[2] G. I. Taylor, Phil. Trans. R. Soc. Lond. Ser. A **223**, 289 (1923).

[3] T. J. Lockett, S. M. Richardson, and W. J. Worraker, J. Non-Newtonian Fluid Mech. **43**, 165 (1992).

[4] B. Alibenyahia, C. Lemaitre, C. Nouar, and N. Ait-Messaoudene, J. Non-Newtonian Fluid Mech. **183**, 37 (2012).

[5] N. Cagney and S. Balabani, Phys. Fluids **31**, 053102 (2019).

[6] V. Sinevic, R. Kuboi, and A. Nienow, Chem. Eng. Sci. **41**, 2915 (1986).

[7] M.-K. Yi and C. Kim, J. Non-Newtonian Fluid Mech. **72**, 113 (1997).

[8] V. K. Gupta, R. Sureshkumar, B. Khomami, and J. Azaiez, Phys. Fluids **14**, 1958 (2002).

[9] M. V. Majji and J. F. Morris, Phys. Fluids **30**, 033303 (2018).

[10] P. Ramesh, S. Bharadwaj, and M. Alam, J. Fluid Mech. **870**, 901 (2019).

[11] J. Gillissen and H. Wilson, Phys. Rev. Fluids **4**, 043301 (2019).

[12] J. Gillissen and H. Wilson, Phys. Rev. E **98**, 033119 (2018).

[13] J. Gillissen and H. Wilson, Phys. Rev. Fluids **4**, 013301 (2019).

[14] J. J. Gillissen, C. Ness, J. D. Peterson, H. J. Wilson, and M. E. Cates, Phys. Rev. Lett. **123**, 214504 (2019).

[15] J. Gillissen, C. Ness, J. Peterson, H. Wilson, and M. Cates, J Rheol. **64**, 353 (2020).

[16] M. E. Ali, D. Mitra, J. A. Schwille, and R. M. Lueptow, Phys. Fluids **14**, 1236 (2002).

[17] R. H. Thomas and K. Walters, J. Fluid Mech. **18**, 33 (1964).

[18] R. G. Larson, E. S. G. Shaqfeh, and S. J. Muller, J. Fluid Mech. **218**, 573 (1990).

[19] A. Groisman and V. Steinberg, Phys. Ref. Lett. **77**, 1480 (1996).

[20] M.-A. Fardin, D. Lopez, J. Croso, G. Grégoire, O. Cardoso, G. McKinley, and S. Lerouge, Phys. Rev. Lett. **104**, 178303 (2010).

[21] N. Liu and B. Khomami, J. Fluid Mech. **737** (2013).

[22] A. M. Philippe, C. Baravian, M. Jenny, F. Meneau, and L. J. Michot, Phys. Rev. Lett. **108**, 254501 (2012).

[23] C. Baravian, D. Vantelon, and F. Thomas, Langmuir **19**, 8109 (2003).

[24] R. DiPrima, P. Eagles, and B. Ng, Phys. Fluids **27**, 2403 (1984).

[25] G. S. Beavers and D. D. Joseph, Phys. Fluids **17**, 650 (1974).

[26] C. S. Dutcher and S. J. Muller, J. Fluid Mech. **641**, 85 (2009).

[27] H. Brenner, Int. J. Multiphase Flow **1**, 195 (1974).

[28] F. Folgar and C. L. Tucker III, J. Reinf. Plast. Compos. **3**, 98 (1984).

[29] E. S. Shaqfeh and G. H. Fredrickson, Phys. Fluids **2**, 7 (1990).

[30] D. L. Koch, Phys. Fluids **7**, 2086 (1995).

[31] C. A. Stover, D. L. Koch, and C. Cohen, J.Fluid Mech. **238**, 277 (1992).

[32] M. Rahnama, D. L. Koch, and E. S. Shaqfeh, Phys. Fluids **7**, 487 (1995).

[33] A. B. D. Brown, S. M. Clarke, P. Convert, and A. R. Rennie, J. Rheol. **44**, 221 (2000).